Switched Capacitor Converter-Based Multi-Port Converter Integrating Bidirectional PWM and Series-Resonant Converters for Standalone Photovoltaic Systems

Masatoshi Uno, *Member, IEEE*, and Kazuki Sugiyama

***Abstract*— Photovoltaic (PV) systems containing a rechargeable battery as an energy buffer require multiple dc-dc converters for PV panel control and battery regulation, and hence, they are prone to be complex and costly. To simplify the system by reducing the number of converters, this paper proposes the non-isolated switched capacitor converter (SCC)-based multi-port converter (SC-MPC) for standalone PV systems. The proposed SC-MPC can be derived by integrating a bidirectional PWM converter, series-resonant converter (SRC), and an SCC with sharing switches. PWM and PFM controls are employed for the PWM converter and SRC, respectively, to regulate either a battery voltage, output voltage, or input power from a PV panel, depending on power balance among the input, battery, and load. The 150-W prototype was built for an experimental verification, and the results demonstrated the output voltage could be regulated independently on the battery voltage or input port of PV panels.**

***Index Terms*—Bidirectional PWM converter, multi-port converter, photovoltaic system, series-resonant converter, switched capacitor converter**

I. Introduction

RENEWABLE energy systems such as photovoltaic (PV) systems require rechargeable batteries for steady power supply by buffering fluctuating power generation of renewable sources. In such systems, multiple dc-dc converters are necessary for not only PV panels but also batteries. A front-end dc-dc converter to perform maximum power point tracking (MPPT) is indispensable to maximize the power generation of PV panels. Meanwhile, a bidirectional dc-dc converter that plays a role of charge-discharge regulation for a battery allows flexible power flows in PV systems. A traditional PV system using an MPPT converter and bidirectional converter for a battery, is illustrated in Fig. 1(a). Although the performance of the system as a whole can be optimized thanks to the two separate converters for different purposes, the system is obviously prone to be complex and costly due to the increased converter count. If these two converters were integrated into one, the system would be simpler at a lower cost by reducing the converter count.

In recent years, multi-port converters (MPCs) have gained considerable attentions in renewable energy applications. MPCs integrate multiple converters into a single unit to reduce the converter count necessary in systems, hence realizing simplified system at a lower cost. A PV system utilizing an MPC is depicted in Fig .1(b).

Various kinds of MPC topologies have been proposed and reported. Isolated MPCs employing a multi-winding transformer are the most straightforward topology—a multi-winding transformer is shared by multiple full- and/or half-bridge converters to have multiple input/output ports [1]–[3]. Multi-winding transformers can easily increase the number of isolated input/output ports. A multi-winding transformer, however, may trigger an increased circuit volume and design difficulty. In addition, these topologies require numerous switches, naturally increasing the circuit complexity and control difficulty.

Partially-isolated MPCs based on the combination of a non-isolated bidirectional PWM converter and an isolated converter have also been proposed [4]–[15]. A switching leg of an isolated converter is shared with that of a non-isolated bidirectional PWM converter, hence reducing the switch count to some extent. Input and output ports of partially-isolated MPCs can be individually controlled by PWM [4]–[6], PFM [7]

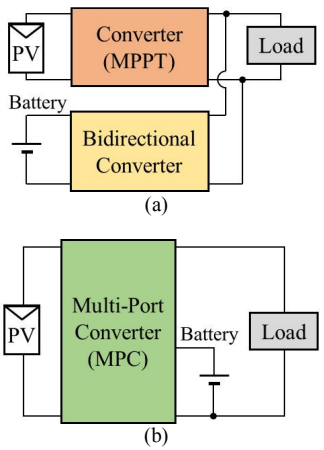

Fig. 1. PV systems based on (a) two separate converters and (b) MPC.

Manuscript received January 13, 2018, revised February 28, 2018; accepted April 5, 2018. This work was supported partly by the Ministry of Education, Culture, Sports, Science, and Technology through Grant-in-Aid for Scientific Research (C) 70443281.

M. Uno is with the Faculty of Engineering, Ibaraki University, Hitachi 316-8511, Japan (e-mail: masatoshi.uno.ee@vc.ibaraki.ac.jp).

K. Sugiyama is with the East Japan Railway Company, Tokyo, Japan (e-mail: sugi.kazu3032@gmail.com).

and/or phase-shift controls [8]–[15].

The isolated and partially-isolated MPCs, however, require an isolation transformer as a key element, and therefore, they are not a preferable topology for non-isolated applications. Non-isolated MPCs are undoubtedly suitable for non-isolated applications. PWM-controlled non-isolated MPCs utilizing a shared dc-link bus is a very simple approach to integrate multiple converters into a single unit [16], [17]. However, since only a few circuit elements are shared among multiple converters, the benefits of the integration are limited. Although many other non-isolated MPC topologies have been proposed, the issues on the shortened effective duty cycle [18], [19] and unshared common ground [20], [21] are cited as top concerns. Meanwhile, PWM-MPCs proposed in [22]–[25] can share switches as well as some passive components between two PWM converters and can operate without suffering from the issues of reduced effective duty cycle nor unshared common ground.

Switched capacitor converters (SCCs), which store energies in capacitors rather than an inductor, have been gaining popularity as high power-density converters realizing reduced circuit volume. In general, an energy density of capacitors is 100 to 1000 times greater than that of inductors [26], [27], and therefore, SCCs achieve circuit miniaturization and higher power density than inductor-based converters. SCCs with no magnetic components, however, are not suitable for applications needing voltage regulation because their power conversion efficiencies severely drop as their voltage conversion ratios move away from a fixed value, and this issue originates from a poor voltage regulation capability of SCCs [28], [29]. Numerous hybrid SCCs employing an additional inductor to achieve PWM [30]–[32], resonant [33]–[36], or phase-shift operations [37] have been proposed to address the issues. In spite of the added inductors, power densities of hybrid SCCs are generally higher than those of ordinary inductor-based converters because a significant part of the whole energy is stored in capacitors rather than inductors [26]. The high power density flying capacitor multilevel inverter has also been demonstrated [38]. With an active energy buffer [39] employing ceramic capacitors, a 2-kW single-phase inverter has achieved a high power density of 216 W/in^3.

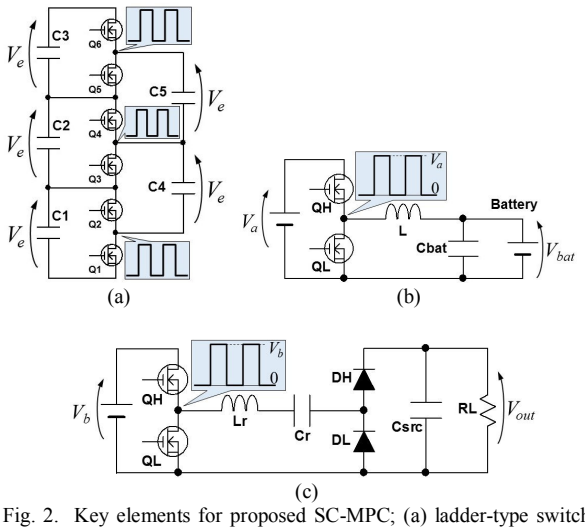

Fig. 2. Key elements for proposed SC-MPC; (a) ladder-type switched capacitor converter (SCC), (b) bidirectional PWM converter, and (c) series-resonant converter (SRC).

To realize high-power density MPCs, this paper proposes a non-isolated SCC-based MPC (SC-MPC) for standalone PV systems. The proposed SC-MPC is derived from the combination of an SCC, bidirectional PWM converter, and series-resonant converter (SRC) with sharing switches. Section II presents the circuit description, operation modes and its power flows, and control block diagram. The detailed operation analyses will be presented in Sections III and IV. In Section V, quantitative analysis based on the charge vector analysis will be performed to determine current stresses of switches in the proposed SC-MPC. The experimental results of a 150-W prototype are presented in Section VI, followed by the comparison between the proposed and conventional MPCs.

II. Switched Capacitor Converter-Based Multi-Port Converter

A. Key Elements for Proposed SC-MPC

The proposed SC-MPC is derived from the combination of three converters shown in Fig. 2—a ladder-type SCC, bidirectional PWM converter, and series-resonant converter (SRC). Since three static capacitors of C_1–C_3 are connected in series in Fig. 2(a), this topology is called 3s-SCC for the sake of convenience. Odd- and even-numbered switches in the SCC [see Fig. 2(a)] are alternately driven, and voltages of all capacitors automatically are unified to be V_e. At the same time, square wave voltages are produced at respective switching nodes, as depicted in the insets in Fig. 2(a).

Meanwhile, in the bidirectional PWM converter shown in Fig. 2(b), the high- and low-side switches Q_H and Q_L are alternately driven to generate a square wave voltage having a peak-to-peak voltage of V_a. The inductor L is charged and discharged as its voltage swings, and a battery voltage V_{bat} can be regulated by adjusting the duty cycle of the generated square wave voltage.

Q_H and Q_L in the SRC shown in Fig. 2(c) are also alternately driven to produce a square wave voltage and to drive the series-resonant tank comprising L_r and C_r. The output voltage V_{out} is controlled by manipulating a switching frequency.

B. Circuit Description of Proposed SC-MPC

The proposed converter can be derived by sharing switches in the three converters listed in Fig. 2. Switches Q_3–Q_4 and Q_5–Q_6 in the SCC are shared with Q_H–Q_L in the bidirectional PWM converter and SRC. The circuit description of the proposed SC-MPC for a non-isolated standalone PV system is shown in Fig. 3. In the SRC, two series-resonant tanks (L_{r1}–C_{r1} and L_{r2}–C_{r2}) are used to reduce an RMS current of each resonant tank, and they are connected to different switching nodes of v_X and v_Y in order to mitigate current stresses of capacitors and switches in the SCC. Two series-resonant tanks are driven by the square wave voltage generated at v_X and v_Y. Meanwhile, the filter inductor L in the PWM converter is driven by the voltage of the switching node v_X. In other words, square wave voltages

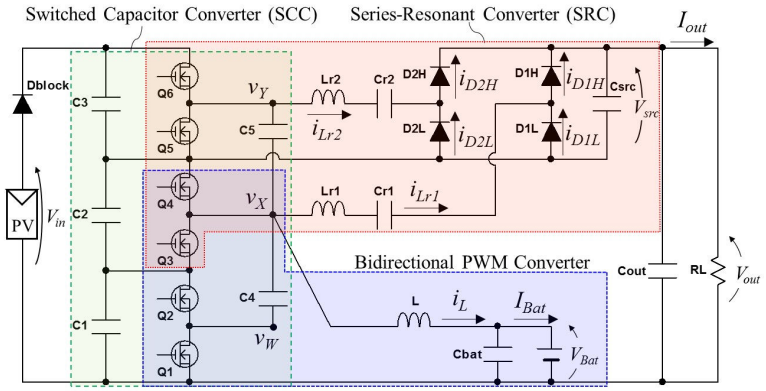

Fig. 3. Proposed switched capacitor converter-based multi-port converter (SC-MPC).

generated in the SCC are utilized not only for the SCC itself but also to drive the SRC and PWM converter.

Since the PWM converter and SRC are integrated, the proposed converter employs two control freedoms of duty cycle d and switching frequency f_S. The battery voltage V_{bat} and output voltage V_{out} are regulated by the PWM converter and SRC, respectively. Meanwhile, the SCC in the SC-MPC behaves as a voltage divider that produces square wave voltages.

In addition to the system simplification by the integration of three circuits (see Fig. 2) into a single unit, the circuit miniaturization thanks to the high-power density characteristic of the SCC [26], [27] is an appealing feature of the proposed SC-MPC. However, the cost is prone to soar as six switches and their gate drivers are necessary. Therefore, the proposed MPC is considered best suitable for applications where system simplification and miniaturization are prioritized over cost reduction. In the following sections, the operation analysis and experimental verification are performed assuming a target application of small satellite power systems with a standard 28-V bus and 14-V rechargeable battery.

C. Operation Modes and Power Flows

Depending on the power balance among the input (i.e., PV panel), battery, and output, the MPC operates either in three operation modes; the single-input dual-output (SIDO) mode, single-input single-output (SISO) mode, and MPPT mode, as shown in Fig. 4. The power balance in the MPC is simply given by

$$P_{in} = P_{out} + P_{bat}, \tag{1}$$

where P_{in}, P_{out}, and P_{bat} are the input, output, and battery charging powers, respectively. This simple equation means that controlling two of three ports automatically determines the rest one. Since two control freedoms of duty cycle d and switching frequency f_S are available for the proposed SC-MPC, PWM and PFM controls are used to regulate two of three ports.

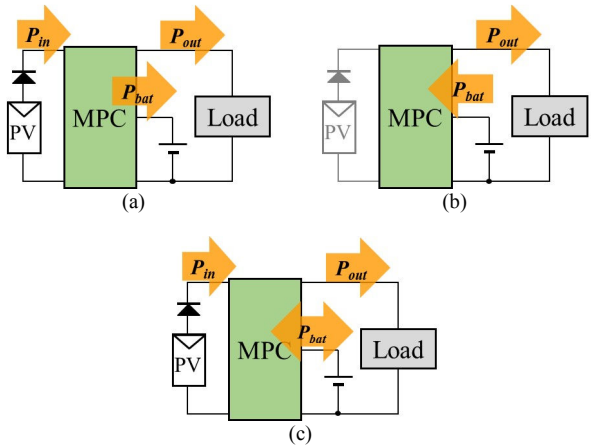

Fig. 4. Power flows in (a) SIDO mode, (b) SISO mode, and (c) MPPT mode.

In the SIDO mode [see Fig. 4(a)], the PV panel is capable of supplying the whole output power, and the surplus power is charged to the battery. V_{out} and V_{bat} are regulated by the SRC and PWM converter, respectively. The detailed operation analysis for the SIDO mode will be performed in Section III.

In the SISO mode [see Fig. 4(b)], the PV panel is not available (e.g., at night), and therefore the battery alone supplies the entire output power (i.e., $P_{out} = -P_{bat}$). The power from the battery flows through not only the PWM converter but also SRC, and hence V_{out} is dependent on both d and f_S. The optimized-f_S PWM control strategy is employed to regulate V_{out} in this paper, as will be discussed in Section IV-A.

In the MPPT mode [see Fig. 4(c)], P_{in} from the PV panels is maximized by the MPPT control, while power surplus or deficit is buffered by the battery. P_{in} is controlled by the PWM converter performing MPPT, while the SRC regulates V_{out} by PFM control. Charging and discharging of the battery is seamlessly switched based on the power balance among three ports.

D. Control

The control block diagram for the proposed MPC is depicted in Fig. 5. V_{out} is always regulated by manipulating the switching frequency f_S in all operation modes, whereas the mode selector is switched to generate the duty cycle of even-numbered switches, d, to regulate either V_{bat} or P_{in}, depending on operation modes. A PI controller generates d to regulate V_{bat} in the SIDO mode, while the MPPT controller adjusts d to maximize P_{in}. In the SISO mode, on the other hand, both f_S and d are manipulated to regulate V_{out}, according to the proposed optimized-f_S PWM control scheme, as will be detailed in Section IV-A.

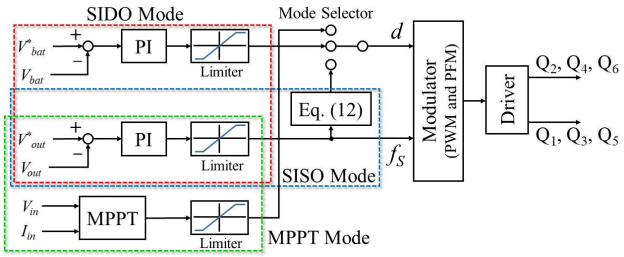

Fig. 5. Control block diagram.

III. Operation Alysis for SIDO Mode

A. Operation Principle in SIDO Mode

In this subsection, the operation analysis in the SIDO mode is performed with the premise that all circuit elements are ideal, two resonant tanks in the SRC have the identical impedance and their currents are uniform, and C_1–C_3 in the SCC equally divide V_{in} into $V_{in}/3$. The resonant frequency f_r is given by

$$f_r = \frac{1}{2\pi\sqrt{L_r C_r}}, \tag{2}$$

where L_r is the inductance of resonant inductors L_{r1} and L_{r2}, and C_r is the capacitance of resonant capacitors C_{r1} and C_{r2}. The key operation waveforms and the current flow directions in the SIDO mode are shown in the Figs. 6 and 7, respectively.

Mode 1 [Fig. 7(a)]: The high-side switches, Q_2, Q_4, and Q_6, are turned-on, and voltages at the switching nodes, v_X and v_Y, are at their high level. C_2 and C_3 are connected in parallel with C_4 and C_5, respectively. The current of L, i_L, linearly increases, and the currents of resonant tanks, i_{Lr1} and i_{Lr2}, start flowing through high-side diodes of D_{1H} and D_{2H}. Mode 1 ends as i_{Lr1} and i_{Lr2} reach zero.

Mode 2 [Fig. 7(b)]: v_X and v_Y are still at their high level, and i_L still linearly increases. Meanwhile, no currents flow in the resonant tanks, and thus, the SRC is essentially inactive in Mode 2. Except for the waveforms in the SRC (i.e., i_{Lr1}, i_{Lr2}, i_{DH}, and i_{DL}), the key operation waveforms in this mode are identical to those in Mode 1.

Mode 3 [Fig. 7(c)]: This mode begins as the low-side switches, Q_1, Q_3, and Q_5, are turned-on, and v_X and v_Y swing to their low level. Accordingly, i_L starts linearly decreasing. In this mode, the combinations of the parallel connections of capacitors are changed; C_1 and C_2 are connected to C_4 and C_5, respectively. i_{Lr1} and i_{Lr2} in the resonant tanks start to flow in the opposite directions as those in Mode 1, and low-side diodes of D_{1L} and D_{2L} conduct. As i_{Lr1} and i_{Lr2} reach zero again, the operation moves to the final mode.

Mode 4 [Fig. 7(d)]: i_{Lr1} and i_{Lr2} become zero again, and therefore, the SRC is inactive in Mode 4. Except for the SRC, the operation of the SC-MPC in this mode is identical to that in Mode 3.

In summary, all the capacitors in the SCC are virtually connected in parallel throughout every switching cycle, and

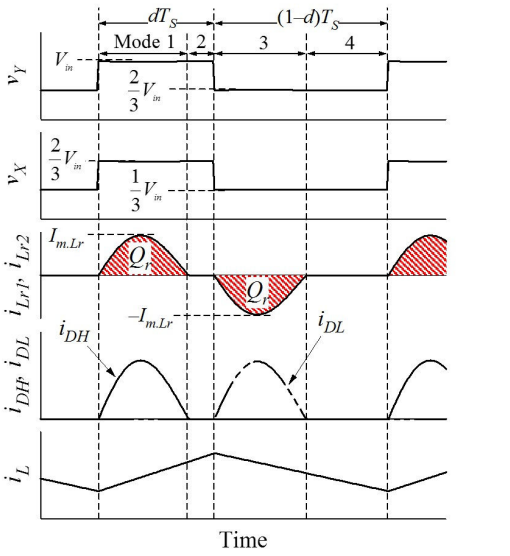

Fig. 6. Key operation waveforms in SIDO mode.

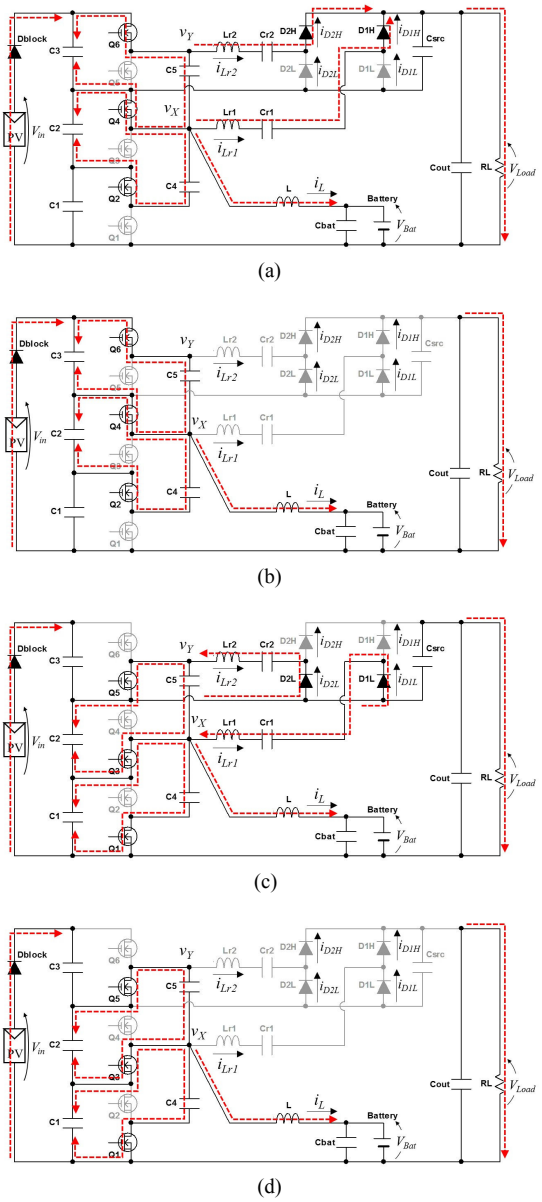

Fig. 7. Current flows in SIDO mode in (a) Mode 1, (b) Mode 2, (c) Mode 3, and (d) Mode 4.

therefore, their voltages are automatically unified. v_X and v_Y swing, and their peak-to-peak voltages are $V_{in}/3$. The square wave voltages of v_X and v_Y are utilized to drive not only L in the PWM converter but also two resonant tanks in the SRC.

B. Operation Criterion

Since the proposed SC-MPC consists of the bidirectional PWM converter and SRC, a cross-regulation between these two converters is of great concern. Specifically, duty cycle variations in the PWM converter may affect the operation of the SRC employing PFM control.

As shown in Figs. 6 and 7, the SRC is basically inactive in Modes 2 and 4, as i_{Lr1} and i_{Lr2} are zero. It suggests that the operation of the SRC is unaffected by duty cycle variation as long as these inactive modes exist. In other words, duty cycle variations are buffered in Modes 2 and 4, and the characteristic of the SRC can be independent on the PWM converter. To this end, half the resonant period ($1/2f_r$) must be shorter than both dT_S and $(1-d)T_S$, where T_S (= $1/f_S$) is the switching period. From this relationship, f_S and f_r need to be designed to fulfill the operation criterion below

$$\frac{f_S}{2f_r} \le d \le 1-\frac{f_S}{2f_r}. \tag{3}$$

The above discussion assumes that shared circuit elements between the bidirectional PWM converter and SRC (i.e., capacitors and switches) are ideal and do not contain parasitic components, such as equivalent series resistance (ESR) and equivalent series inductance (ESL). In reality, however, capacitors and switches are non-ideal, and therefore, slight cross-regulation between the bidirectional PWM converter and SRC is anticipated due to non-negligible parasitic components. The experimental tests were performed to investigate whether operations of these two converters were independent. The results will be shown in Section VI-C.

C. Bidirectional PWM Converter

The proposed converter employs PWM control to regulate the battery voltage V_{bat}. As aforementioned, voltages of C_1–C_3 can be assumed to be $V_{in}/3$ because the SCC behaves as an ideal voltage divider. Meanwhile, L is connected to the switching node of v_X, at which the voltage swings between $2/3V_{in}$ and $V_{in}/3$ (see Fig. 6). From the volt-second balance on L, the voltage conversion ratio of the PWM converter, M_{bat}, is yielded as

$$M_{bat} = \frac{V_{bat}}{V_{in}} = \frac{1+d}{3}. \tag{4}$$

Although L is connected to the node of v_X in Fig. 3, other switching nodes v_W and v_Y can also be used to drive L. Connecting L to the nodes of v_W and v_Y yields voltage conversion ratios of $M_{bat} = d/3$ and $(2+d)/3$, respectively. Thus, a proper switching node should be selected so that M_{bat} satisfies requirements.

M_{bat} of (4) indicates that the theoretical voltage regulation range is between $V_{in}/3$ and $2V_{in}/3$, and is one-third of that of traditional PWM converters. This is because V_{in} is divided into three by the SCC, and the voltage swing with a peak-to-peak value of $V_{in}/3$ is used to drive L. With a 2s-SCC, in which two static capacitors are connected in series, the peak-to-peak voltage at a switching node is increased to $V_{in}/2$, and hence the voltage regulation range can be extended to half that of traditional PWM converters. An example of the 2s-SCC-based topology with a single resonant tank will be shown in Appendix.

D. Series Resonant Converter (SRC)

The proposed SC-MPC also utilizes PFM control to regulate the output voltage V_{out}—the SRC in the SC-MPC regulates V_{out} by adjusting f_S. Ordinary resonant converters, including SRCs, operate with f_S higher than f_r to ensure soft-switching operations. The SRC in the proposed SC-MPC, on the other hand, is designed so that f_r is higher than f_S to achieve the duty-independent operation of the SRC, as explained in Section III-B.

The operation analysis for the SRC is performed with the equivalent circuit shown in Fig. 8. Since the two resonant tanks are driven by square waves having the same peak-to-peak voltage of $V_{in}/3$ (see Fig. 6), they can be merged into a single resonant tank in Fig. 8. By neglecting the inactive periods of Modes 2 and 4, the analysis can be dramatically simplified. Based on the fundamental harmonics approximation (FHA), the square wave voltage of v_{sw}, which corresponds to v_X and v_Y in Fig. 3, and v_{rec} can be approximated to be sinusoidal waves as

$$\begin{cases} v_{sw} = V_{m.sw}\sin\omega_r t = \dfrac{2}{\pi}\dfrac{1}{3}V_{in}\sin\omega_r t \\ v_{rec} = V_{m.rec}\sin\omega_r t = \dfrac{2}{\pi}\left(V_{src}+2V_f\right)\sin\omega_r t \end{cases}, \tag{5}$$

where $V_{m.sw}$ and $V_{m.rec}$ are the amplitude of v_{sw} and v_{rec}, V_f is the forward voltage drop of diodes, and V_{src} is the voltage of C_{src}. The current amplitude of i_{Lr} (see Fig. 6), $I_{m.Lr}$, can be yielded as

$$I_{m.Lr} = \frac{V_{m.sw}-V_{m.rec}}{|Z|} = \frac{\frac{2}{\pi}\left\{\frac{V_{in}}{3}-\left(V_{src}+2V_f\right)\right\}}{R_{res}}, \tag{6}$$

where Z and R_{res} are the characteristic impedance and total resistance of the resonant tank, respectively. The charge delivered by C_r, Q_r (see Fig. 6), is expressed as

$$Q_r = \int_0^{0.5T_r} I_{m.Lr}\sin\omega_r t dt = \frac{1}{\pi f_r} I_{m.Lr}. \tag{7}$$

Since two resonant tanks are utilized in the proposed SC-MPC, the total amount of the charge in a single switching cycle

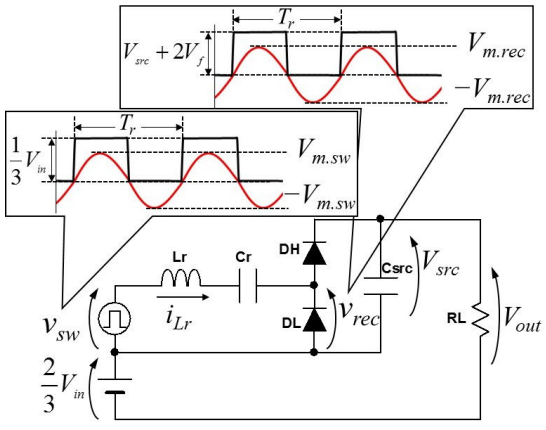

Fig. 8. Equivalent circuit and approximated waveforms of SRC.

is $2Q_r$. The average output current I_{out} can be expressed as

$$I_{out} = \frac{2Q_r}{T_S} = 2\frac{f_S}{\pi f_r} I_{m.Lr}. \quad (8)$$

Substitution of (8) into (6) with the relationships of $V_{out} = I_{out} \times R_L$ and $V_{src} = V_{out} - 2V_{in}/3$ yields

$$V_{out} = \frac{1}{1+\frac{\pi^2}{4}\frac{f_r}{f_S}\frac{R_{res}}{R_L}}\left(V_{in} - 2V_f\right). \quad (9)$$

To fairly discuss the voltage conversion characteristics of the SRC with respect to f_S, the normalized switching frequency F is defined as

$$F = \frac{f_S}{f_r}. \quad (10)$$

From (9) and (10), the voltage conversion ratio of the SRC, M_{out}, is yielded as

$$M_{out} = \frac{V_{out}}{V_{in}} = \frac{1}{1+\frac{\pi^2}{4F}\frac{R_{res}}{R_L}}\left(1 - \frac{2V_f}{V_{in}}\right). \quad (11)$$

The above analysis and M_{out} of (11) are for the case that C_{scr} is stacked on C_2, and the sum voltage of C_1 and C_2 (i.e., $2V_{in}/3$) contributes to V_{out}, as can be seen in Fig. 8. By stacking C_{scr} on other static capacitors (i.e., C_1 or C_3) or the ground, M_{out} as well as its regulation range can be modified. Hence, C_{scr} should be stacked on a proper static capacitor according to applications and requirements. Appendix section exemplifies the case that C_{scr} is grounded in the 2s-SCC-based SC-MPC.

IV. Operation in SISO and MPPT Modes

A. Optimized Switching Frequency PWM Control in SISO Mode

In the SISO mode, the battery alone supplies the whole output power through the PWM converter and SRC in the proposed SC-MPC. In other words, two control freedoms of d and f_S are available to regulate V_{out}. In the SIDO mode, the SC-MPC operates so that inactive periods of the SRC exist to achieve the independent voltage regulation for V_{out} and V_{bat}, as discussed in the previous section. These inactive periods, however, naturally increase RMS currents and Joule losses in the SRC, hence likely decreasing a power conversion efficiency.

With the proposed optimized-f_S PWM control scheme, V_{out} is basically regulated with PWM control, while f_S is varied to eliminate one of these inactive periods. Specifically, f_S is adjusted so that dT_S or $(1-d)T_S$ be equal to $1/2f_r$, as

$$f_S = 2f_r\{0.5 - |d - 0.5|\}. \quad (12)$$

The key operation waveforms and the current flows in the SISO mode at d = 0.4 are shown in the Figs. 9 and 10, respectively. Thanks to the blocking diode D_{block}, reverse power flow to the PV panel is prevented. In comparison with the SIDO mode shown in Fig. 7, there are fewer operation modes as one of the inactive periods disappears. According to (12), no inactive periods exist at d = 0.5, and currents in the SRC can be continuous.

Equations derived in the previous section for the SIDO mode can be used to obtain V_{out} in the SISO mode. Eliminating V_{in} from (4), (9), and (10) yields

$$V_{out} = \frac{1}{1+\frac{\pi^2}{4F}\frac{R_{res}}{R_L}}\left(\frac{3V_{bat}}{1+d} - 2V_f\right). \quad (13)$$

B. Operation in MPPT Mode

Except for control objectives, key waveforms and current

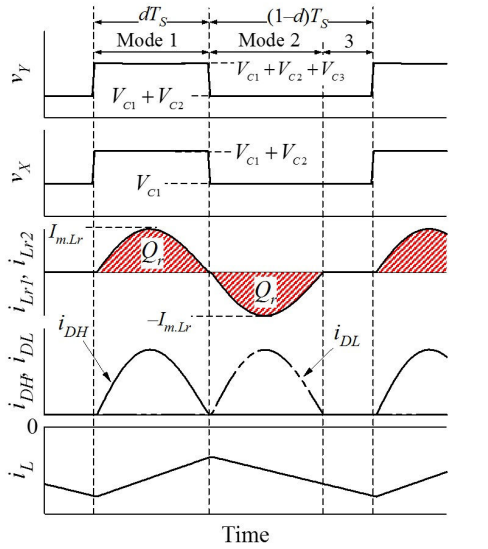

Fig. 9. Key operation waveforms in battery mode (d = 0.4).

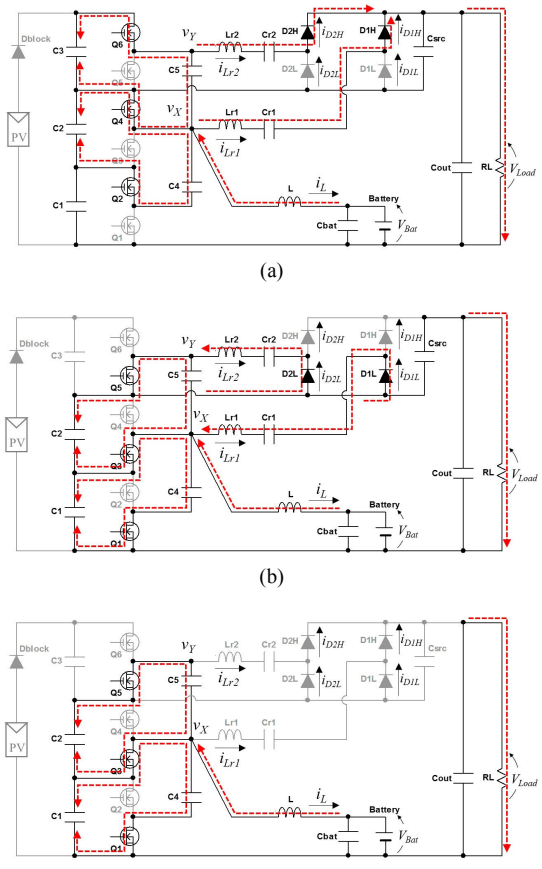

Fig. 10. Current flows in SISO mode (d = 0.4) in (a) Mode 1, (b) Mode 2, and (c) Mode 3.

flow directions in the MPPT mode are identical to those in the SIDO mode. Hence, waveforms and operation modes in the MPPT mode are not illustrated to save page length. The PWM converter maximizes P_{in} based on the MPPT control, while the SRC regulates V_{out} with PFM control. The battery buffers power surplus or deficit, and the power flow direction of the battery is seamlessly switched depending on power balance among three ports.

V. Quantitative Analysis

A. Charge Vector Analysis

In general, capacitors in SCCs deliver a unique amount of charge depending on their positions, structures, and input/output currents. Determination of current stresses of semiconductor devices is crucial to design the proposed SC-MPC. In this section, the charge vector analysis [40], [41] that is based on the Kirchhoff's current law (KCL) is performed to determine the unique amount of delivered charge. A time constant of capacitors ($\tau = CR$) is assumed to be large enough compared to T_S so that current waveforms in the SCC are approximated as square waves [42], [43].

The proposed SC-MPC operates either in the SIDO, SISO, and MPPT modes, as discussed in Section II. As a representative case, the SIDO mode consisting of four operation modes, including inactive periods of the SRC (see Fig. 7), is analyzed. To simplify the charge vector analysis, the resonant currents are approximated to be square wave currents, as shown in Fig. 11. This current approximation reduces the number of operation modes from four to two. From (7), I_{avg1} and I_{avg2} of the approximated square wave currents (as designated in Fig. 11) are given by

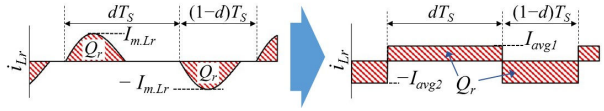

Fig. 11. Notional image of resonant current approximation.

$$\begin{cases} I_{avg1} = \dfrac{Q_r}{dT_S} = \dfrac{1}{\pi d} FI_{m.Lr} \\ I_{avg2} = \dfrac{Q_r}{(1-d)T_S} = \dfrac{1}{\pi(1-d)} FI_{m.Lr} \end{cases} . \tag{14}$$

The charge flows in each switching mode are defined as shown in Fig. 12. Two resonant tanks are assumed to deliver the same amount of charge $q_r = Q_r/T_S$. The even-numbered switches are on in Mode H, and the KCL at nodes A–D [see Fig. 12(a)] yields the following set of equations;

$$\begin{cases} 0 = -q_{C3} - q_{C5} - q_r + dI_{in} \\ 0 = -q_{C2} + q_{C3} - q_{C4} + q_{C5} - q_r + q_{src} - dI_{bat} \\ 0 = -q_{C1} + q_{C2} + q_{C4} \\ 0 = 2q_r - q_{src} - dI_{out} \end{cases} . \tag{15}$$

The odd-numbered switches are on in Mode L, and the KCL at nodes A'–D' [see Fig. 12(b)] yields

$$\begin{cases} 0 = q_{C3} + (1-d)I_{in} \\ 0 = q_{C2} - q_{C3} + q_{C5} - q_r - q_{src} \\ 0 = q_{C1} - q_{C2} + q_{C4} - q_{C5} + q_r - (1-d)I_{bat} \\ 0 = q_{src} - (1-d)I_{out} \end{cases} . \tag{16}$$

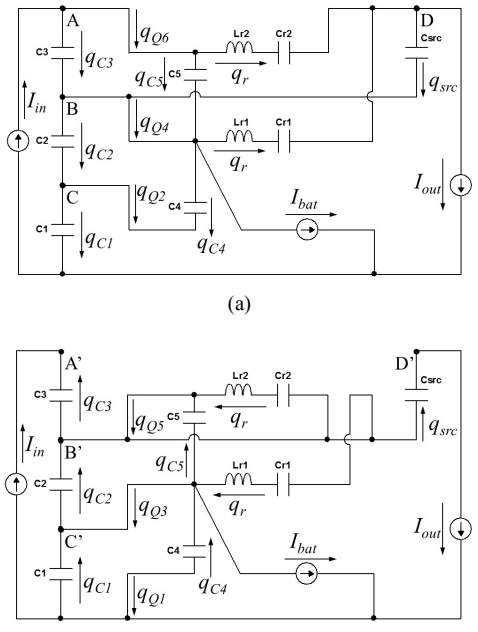

(a)

(b)

Fig. 12. Charge flows in (a) Mode H and (b) Mode L.

The amount of charge flowing through switches can be yielded as

$$\begin{cases} q_{Q1} = -q_{C4} \\ q_{Q2} = -q_{C4} \\ q_{Q3} = -q_{C1} + q_{C2} \\ q_{Q4} = -q_{C2} + q_{C3} + q_{src} \\ q_{Q5} = q_{C5} + q_r \\ q_{Q6} = q_{C5} + q_r \end{cases} . \tag{17}$$

From (15) and (16),

$$\begin{bmatrix} 0 \\ 0 \\ 0 \\ 0 \\ 0 \\ 0 \\ 0 \\ 0 \\ I_{bat} \\ I_{out} \end{bmatrix} = \begin{bmatrix} 0 & 0 & -1 & 0 & -1 & -1 & 0 & d & 0 & 0 \\ 0 & -1 & 1 & -1 & 1 & -1 & 1 & 0 & -d & 0 \\ -1 & 1 & 0 & 1 & 0 & 0 & 0 & 0 & 0 & 0 \\ 0 & 0 & 0 & 0 & 0 & 2 & -1 & 0 & 0 & -d \\ 0 & 0 & 1 & 0 & 0 & 0 & 0 & d' & 0 & 0 \\ 0 & 1 & -1 & 0 & 1 & -1 & -1 & 0 & 0 & 0 \\ 1 & -1 & 0 & 1 & -1 & 1 & 0 & 0 & -d' & 0 \\ 0 & 0 & 0 & 0 & 0 & 0 & 1 & 0 & 0 & -d' \\ 0 & 0 & 0 & 0 & 0 & 0 & 0 & 0 & 1 & 0 \\ 0 & 0 & 0 & 0 & 0 & 0 & 0 & 0 & 0 & 1 \end{bmatrix} \begin{bmatrix} q_{C1} \\ q_{C2} \\ q_{C3} \\ q_{C4} \\ q_{C5} \\ q_r \\ q_{src} \\ I_{in} \\ I_{bat} \\ I_{out} \end{bmatrix} \tag{18}$$

where $d' = (1 - d)$. From (18), the current of capacitors I_{Ci}, (i = 1…5) can be obtained as

$$I_{Ci} = \begin{cases} \dfrac{q_{Ci}}{d} & (\text{Mode H}) \\ \dfrac{q_{Ci}}{1-d} & (\text{Mode L}) \end{cases} . \tag{19}$$

From (17) and (18), the current of switches I_{Qj} (j = 1…6) can be expressed as

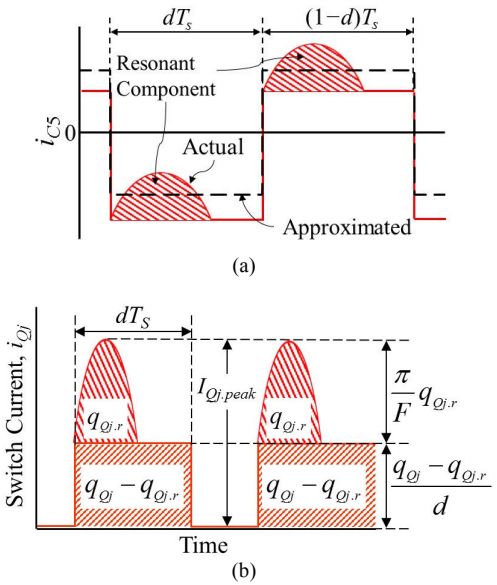

Fig. 13. (a) Actual and approximated current waveforms of i_{C5}, (b) switch current waveform containing resonant and square wave components (even-numbered switches).

$$I_{Qj}=\begin{cases}\dfrac{q_{Qj}}{d} & (\text{for } Q_2, Q_4, Q_6)\\ \dfrac{q_{Qj}}{1-d} & (\text{for } Q_1, Q_3, Q_5)\end{cases}. \tag{20}$$

Similarly,

$$\begin{cases} I_{\text{avg1}}=\dfrac{q_r}{d} \\ I_{\text{avg2}}=\dfrac{q_r}{1-d}\end{cases}. \tag{21}$$

B. Peak Current of Switches

In the previous subsection, sinusoidal resonant currents were approximated to be square wave currents in order to perform the charge vector analysis. Therefore, the current values determined in the previous subsection are somewhat lower than actual peak currents. For instance, the actual and approximated current waveforms of C_5, i_{C5}, are compared in Fig. 13(a). Although the delivered charge amounts are identical in both waveforms, their peak currents as well as RMS values are different. Switches also experience larger peak currents, as illustrated in Fig. 13(b). Determination of the peak current values of switches is essential for a circuit design process.

Since the charge amount of the resonant components, $q_r = Q_r/T_S$, has already been determined in the previous subsection, correct peak currents of switches can be calculated by separating and recalculating resonant components using (14). The amount of charge delivered through the switch Q_j, q_{Qj} [see (17)], is decomposed into a resonant component of $q_{Qj.r}$ and a square wave component of $q_{Qj} - q_{Qj.r}$, as designated in Fig. 13(b). Consequently, a peak current value $I_{Qj.peak}$ is yielded from the sum of the resonant and square wave current calculated from $q_{Qj.r}$ and $q_{Qj} - q_{Qj.r}$, respectively. To this end, charge flows of resonant components are focused, as shown in Fig. 14, in which square wave components are not illustrated for the sake of clarity.

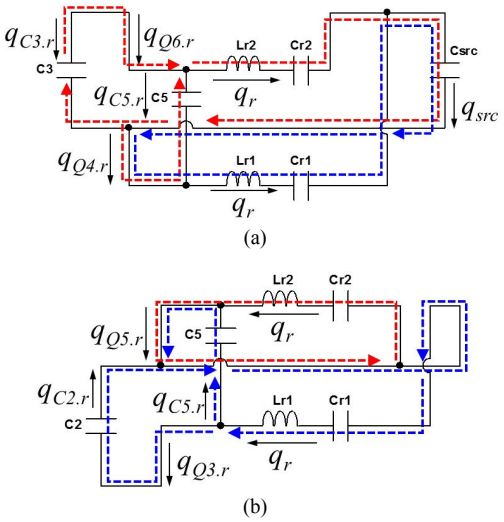

Fig. 14. Charge flows of resonant components in (a) Mode H and (b) Mode L.

In Mode H, q_r of the resonant tank L_{r2}-C_{r2} is delivered from C_3 and C_5, while q_r of the resonant tank L_{r1}-C_{r1} circulates, as shown in Fig. 14(a). In Mode L, on the other hand, q_r of the resonant tank L_{r2}-C_{r2} circulates, while q_r of L_{r1}-C_{r1} is equally divided into C_2 and C_5. In summary, the charges of the resonant components are expressed as

$$\begin{cases} q_{C3.r}=q_{C5.r}=\dfrac{q_r}{2}(\text{Mode H}) \\ q_{C2.r}=q_{C5.r}=\dfrac{q_r}{2}(\text{Mode L})\end{cases}, \tag{22}$$

where $q_{Ci.r}$ is the resonant component in q_{Ci}. From (22) and charge flow directions, as shown in Fig. 14, the resonant component in q_{Qj}, $q_{Qj.r}$, can be expressed as

$$\begin{cases} q_{Q1.r}=q_{Q2.r}=0 \\ q_{Q3.r}=q_{Q6.r}=\dfrac{q_r}{2} \\ q_{Q4.r}=q_{Q5.r}=\dfrac{3q_r}{2}\end{cases}. \tag{23}$$

Now, q_{Qi} can be decomposed to the resonant component of $q_{Qj.r}$ and square wave component of $q_{Qj} - q_{Qj.r}$. From (17) and (23), the peak current of switch Q_j, $I_{Qj.peak}$, can be obtained as

TABLE I
CONDITIONS FOR QUANTITATIVE COMPARISON ON SWITCH CURRENT STRESSES

Switch	SIDO	SISO	MPPT
V_{in} [V]	30		30
I_{in} [A]	—		1.67
I_{out} [A]	3.57	3.57	3.57
V_{out} [V]	≈ 28	≈ 28	≈ 28
V_{bat} [V]	16	16	16
I_{bat} [A]	3.125	—	—
d	0.6	0.6	0.6
F	0.61	0.8	0.61

TABLE II
SWITCH CURRENT STRESSES IN EACH OPERATION MODE

Switch	SIDO	SISO	MPPT
Q_1	−3.65 (−3.7)	7.81 (8.0)	4.15 (4.2)
Q_2	−2.43 (−2.5)	5.2 (5.5)	2.77 (2.8)
Q_3	−5.88 (−5.9)	9.08 (9.1)	6.52 (6.5)
Q_4	12.12 (12.2)	−10.41 (−10.6)	6.18 (6.1)
Q_5	20.21 (20.2)	−6.69 (−6.8)	11.29 (11.2)
Q_6	11.84 (11.9)	2.02 (2.0)	5.9 (5.9)

†All values are in ampere
†Theoretical model (simulation)

$$I_{Qj.peak} = \begin{cases} \dfrac{q_{Qj.r} - q_{Qj.r}}{d} + \dfrac{\pi}{F} q_{Qj.r} & (Q_2, Q_4, Q_6) \\ \dfrac{q_{Qj.r} - q_{Qj.r}}{1-d} + \dfrac{\pi}{F} q_{Qj.r} & (Q_1, Q_3, Q_5) \end{cases}. \quad (24)$$

C. Comparison on Switch Current Stresses

The current stresses determined from the derived theoretical model (24) are compared with those in the simulation in the SIDO, SISO, and MPPT modes. Conditions for the comparative analysis are listed in Table I. Circuit elements used for a 150-W prototype (see Table III) were applied in the simulation analysis. In all operation modes, current sources were used for regulated ports, whereas a voltage source was applied to an unregulated port. For example, the battery and output ports were a current source in the SIDO mode, in which the battery and output are regulated. Although simulation analyses were performed with open-loop control, V_{out} was nearly 28 V, which corresponded to a target voltage and maximum P_{out} of 100 W in the experiment (see Section VI).

The results of the quantitative comparison are shown in Table II. In all operation modes, the derived theoretical model and simulation result (values in parentheses) matched very well with errors lower than a few percent, verifying the derived model in the previous subsection.

Depending on operation modes, switches experience different peak current stresses, and therefore, switches must be designed to fulfill the largest current stress. The largest peak current of each switch among three modes are highlighted with grey in Table II. Since both P_{out} and P_{bat} are supplied from the input port, top three switches (Q_4–Q_6), which are located near the input port, experience large current stresses. In the SISO mode, on the other hand, P_{out} is supplied from the battery port, and therefore, current stresses of bottom three switches (Q_1–Q_3), which are placed near the battery port, become significant. In the MPPT mode, since P_{out} is supplied from both the battery and input, all current stresses are moderate.

VI. EXPERIMENTAL RESULTS

A. Prototype

A 150-W prototype of the proposed SC-MPC for P_{out} = 100 W and P_{bat} = 50 W was built, as shown in Fig. 15, for a power system of small satellites with a 28-V bus and 14-V rechargeable battery. A circuit element list is shown in Table III. The prototype was operated with V_{in} = 30 V, V_{out} = 28 V, and V_{bat} = 12–16 V. The resonant frequency f_r was 164 kHz.

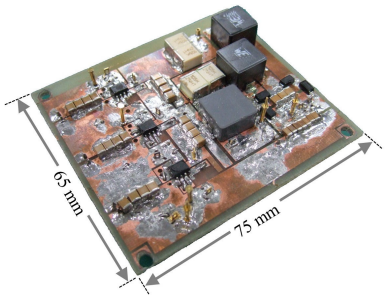

Fig. 15. Photograph of 150-W prototype.

TABLE III
CIRCUIT ELEMENT LIST

Element	Value
Q_1–Q_6	Dual MOSFET, IRF7905, R_{on} = 21.8 and 17.1 m Ω for high- and low-side switches
C_1–C_5	Ceramic Capacitor, 47 µF × 4
L_{r1}, L_{r2}	0.47 µH
C_{r1}, C_{r2}	Film Capacitor, 1.0 µF × 2
D_{H1}, D_{H2}, D_{L1}, D_{L2}	Schottky Diode, RSX501L-20TE25, V_f = 0.39 V
C_{src}	Ceramic Capacitor, 47 µF × 3
C_{out}	Ceramic Capacitor, 10 µF × 7
C_{bat}	Ceramic Capacitor, 22 µF × 5
L	33 µH
Gate Driver	MCP14628

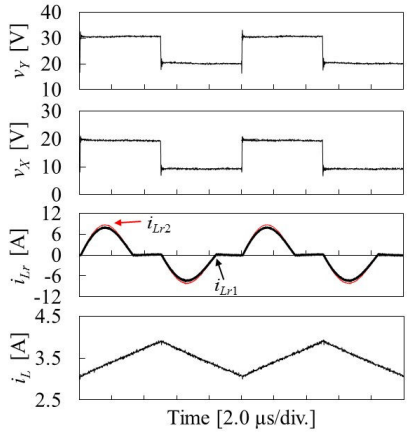

(a)

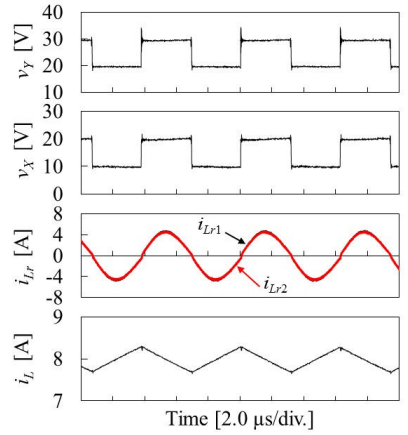

(b)

Fig 16. Measured key waveforms in (a) SIDO mode and (b) SISO mode (d = 0.5).

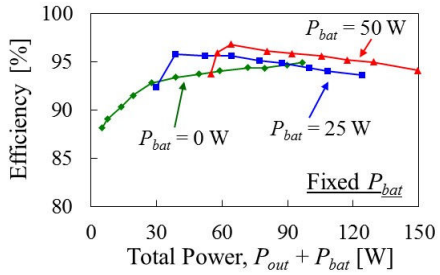

(a)

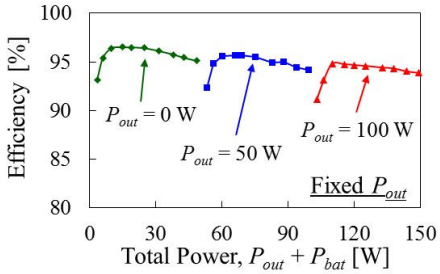

(b)

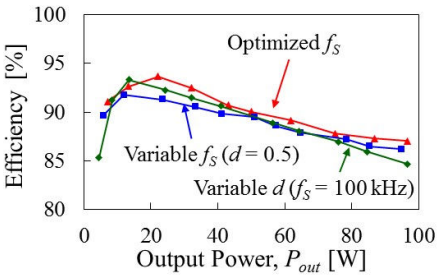

(c)

Fig. 17. Measured power conversion efficiencies in (a) SIDO mode at fixed P_{bat}, (b) SIDO mode at fixed P_{out}, and (c) SISO mode.

The prototype was controlled by PE-Expert 4 employing TMS320C6657 (Myway Plus Corporation, Japan).

B. Waveforms and Efficiencies

Measured key operation waveforms in the SIDO mode (P_{out} = 100 W and P_{bat} = 50 W) and in the SISO mode (P_{out} = 100 W) are shown in Figs. 16(a) and (b), respectively. The imbalances between i_{Lr1} and i_{Lr2} attributable to a slight impedance mismatch between two resonant tanks were observed in both modes. Voltage spikes due to parasitic inductances were observed in both operation modes, and Fig. 16(b) showed greater overshoot. The difference in voltage spikes between SIDO and SISO modes probably arose from the different conditions of switch current, as suggested in Table II—current peaks and directions significantly vary depending on operation modes. The measured waveforms agreed well with the theoretical ones, verifying the operation of the proposed SC-MPC.

Measured power conversion efficiencies in the SIDO mode as a function of the total power of P_{out} + P_{bat} are shown in Fig. 17 (a) and (b). The efficiencies at a full load of 150 W were as high as 94%. Meanwhile, when P_{bat} = 0 W [see Fig. 17(a)], the prototype operated as an SC-SRC alone, and its efficiency was approximately 95% at 100 W. Similarly, when P_{out} = 0 W [see Fig. 17(b)], the circuit behaved as an SC-PWM converter, and its efficiency was 95% at 50 W. In comparison with reported efficiencies of 97% and 90% of conventional PWM [30] and resonant SCCs [36], respectively, the measured efficiencies of the prototype are considered appropriate.

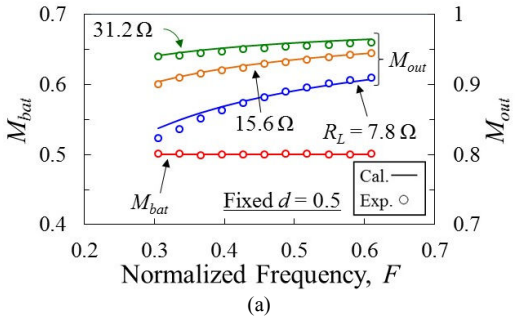

(a)

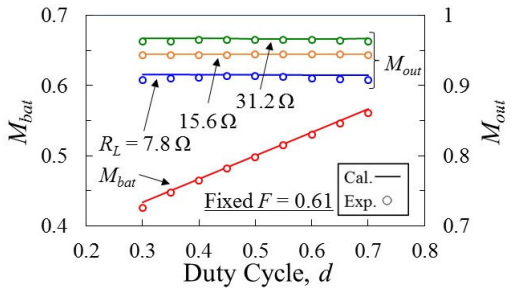

(b)

Fig. 18. Measured voltage conversion characteristics as a function of (a) normalized switching frequency F and (b) duty cycle d.

Power conversion efficiencies in the SISO mode with the proposed optimized-f_S PWM control technique were measured, as shown in Fig. 17(c). Efficiencies with a fixed d = 0.5 or fixed f_S = 100 kHz (F = 0.61) were also measured for comparison. With the optimized-f_S PWM control, power conversion efficiencies were improved by a few percent, demonstrating the efficacy of the proposed switching strategy.

C. Voltage Conversion Ratios and Interdependence between Output and Battery Voltages in SIDO Mode

The interdependence between V_{out} and V_{bat} in the SIDO mode was investigated. Voltage conversion ratios of M_{bat} and M_{out}, which were defined by (4) and (11), were measured with varying F or d, as shown in Fig. 18. Measured characteristics matched well with the theoretical voltage conversion ratios of (4) and (11). Characteristics of M_{out} and M_{bat} were dependent and independent on F, respectively, as shown in Fig. 18(a). On the other hand, M_{bat} showed a linear relationship with d, while characteristics of M_{out} were constant, as shown in Fig. 18(b). In both cases, M_{out} was dependent on the value of R_L, as (11) indicated. These results suggest that M_{bat} and M_{out} (i.e., V_{bat} and V_{out}) can be independently regulated with PWM and PFM controls.

Transient response characteristics in the SIDO mode were measured to demonstrate the decoupled output regulation. V_{out} and V_{bat} were regulated to be 28 V and 16 V, respectively, while

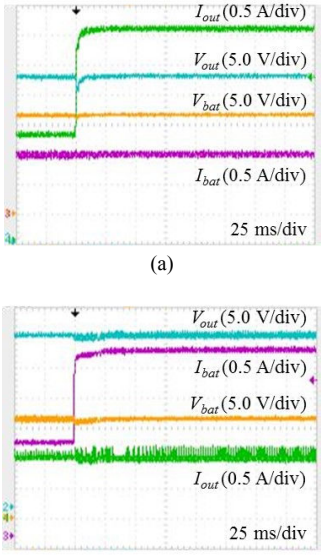

Fig. 19. Measured transient response characteristics during (a) step-change in I_{out} and (b) step-change in I_{bat}.

I_{out} or I_{bat} was step-changed. The measured response characteristics are shown in Fig. 19. V_{out} slightly dropped in response to the step change in I_{out}, as shown in Fig.19(a). Meanwhile, V_{bat} was unaffected by the change in I_{out}, demonstrating that PWM-controlled V_{bat} was independent on PFM-controlled V_{out}. Similar results were observed in the case of the step change in I_{bat}, as shown in Fig. 19(b)—the influence of the step change in I_{bat} was very trivial to V_{out}. The results demonstrated V_{out} and V_{bat} could be independently regulated by PFM and PWM controls, respectively, even during transients.

D. Power Balance Test with MPPT Control

A power balance test in the MPPT mode was performed. A solar array simulator (E4361A, Keysight Technologies) was used as the input source instead of a real PV panel, and its maximum power was set to be 50 W. Perturb and observation (P&O) algorithm-based MPPT was performed by PWM control. V_{out} was regulated to be 28 V by PFM control, and P_{out} was manually varied between 40 W to 60 W.

Measured P_{in}, P_{out}, and P_{bat} are shown in Fig. 20. The battery was charged in Periods 1 and 3 when $P_{in} > P_{out}$. In Period 2 ($P_{in} < P_{out}$), on the other hand, the battery started discharging to meet the power balance. In summary, P_{in} was kept to be 50 W by MPPT control, while the battery was charged and discharged depending on the relationship between P_{in} and P_{out}.

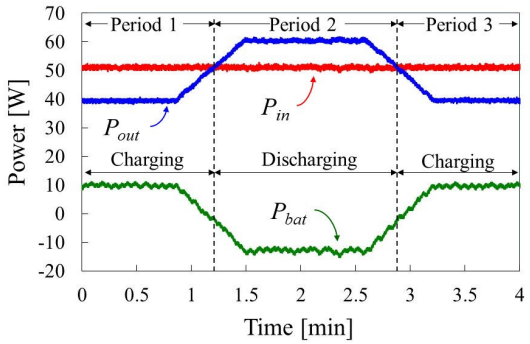

Fig. 20. Experimental results of power balance test with MPPT control.

VII. Comparison

The proposed SC-MPC is compared with conventional representative non-isolated MPCs from various aspects, including component counts, control scheme, decoupled regulation capability, and reported full load efficiency. In addition, voltage conversion ratios and duty cycle limitation are also compared—it is noted that duty cycles, d_1 and d_2, are arbitrary chosen, and therefore, these symbols are different from those used in original papers. For fair comparison, topologies with the issues of reduced effective duty cycle or unshared ground are excluded.

Conventional non-isolated MPCs employ PWM control scheme, and are not capable of decoupled output voltage regulation (e.g., Conversion Ratios 2 of some topologies contain both d_1 and d_2). The proposed SC-MPC, on the other hand, exploits both PWM and PFM controls, and offers decoupled regulation, as discussed and demonstrated in Sections III-B and VI-C as long as (3) is satisfied. As for full load power conversion efficiencies, the proposed MPC is comparable to conventional ones.

The proposed SC-MPC requires numerous switches and capacitors due to the ladder-type SCC-based topology, and therefore, it is prone to be complex and costly. Furthermore, the voltage conversion ranges are relatively narrow because the divided voltage is used to drive the inductor and resonant tanks,

TABLE IV
Comparison among non-isolated MPCs.

Topology	Component Count				Control Scheme	Decoupled Regulation	Full Load Efficiency	Conversion Ratios		Duty Cycle Limitation
	Switch	D	L	C				1	2	
[17]	6	0	2	3	PWM	No	94%	$\frac{d_1}{1-d_1}$	$\frac{d_2}{1-d_1}$	$d_2 > d_1$
[22]	3	1	3	4	PWM	No	97%	$\frac{1}{1-d_1}$	$\frac{1-d_2}{1-d_1}$	$d_1 > d_2$
[24]	3	0	2	3	PWM	Yes	Not reported	$\frac{1}{1-d_1}$	$\frac{1}{1-d_2}$	$d_2 > d_1$
[25]	3	1	2	4	PWM	No	97%	$\frac{1}{2-d_1}$	$\frac{d_2}{2-d_1}$	$d_1 > d_2$
Proposed	6	4	3	10	PWM PFM	Yes	94%	$\frac{1+d_1}{3}$	Eq. (11)	Eq. (3)

as discussed in Sections III-C and -D. In spite of these drawbacks, the major advantage of the reduced circuit volume thanks to the SCC structure would be attractive for applications where circuit miniaturization is of primary importance (e.g., satellite power systems).

VIII. Conclusions

The non-isolated SC-MPC for standalone PV systems has been proposed in this paper. The proposed MPC can be derived by integrating a ladder-type SCC, bidirectional PWM converter, and SRC into a single unit with sharing switches. Square wave voltages generated at switching nodes in the SCC are utilized to drive series-resonant tanks in the SRC and a filter inductor in the PWM converter. The proposed SC-MPC employs not only PFM control for output voltage regulation but also PWM control for battery voltage regulation or MPPT for PV panels.

Detailed operation analyses were performed, based on which the theoretical model of the proposed SC-MPC was derived. In addition, the charge vector analysis was also performed to determine the amount of charge flowing through respective capacitors in the SCC as well as peak current stresses of switches. The characteristics of the derived model matched very well with simulation and experimental results, verifying the derived mathematical model.

The 150¬-W prototype was built, and experimental verification tests were performed. The measured power conversion efficiency at the rated power was as high as 94%. The measured voltage conversion and transient response characteristics demonstrated that the output and battery voltages could be independently regulated by PFM and PWM controls, respectively, without being interfered each other.

Appendix

As mentioned in Sections III-C and -D, the voltage regulation ranges of M_{bat} and M_{out} are dependent on not only the structure of the SCC but also positions at which L and C_{src} are connected. In the case of the SC-MPC based on the 2s-SCC shown in Fig. 21, V_{in} is divided into two by C_1 and C_2, and the node voltage v_X swings between $V_{in}/2$ and V_{in}. Since L is connected to the node v_X, M_{bat} is given by

$$M_{bat} = \frac{1+d}{2} \tag{25}$$

Meanwhile, C_{src} is grounded, and V_{out} is equal to V_{src}. From the analysis in Section III-D, M_{out} is yielded as

$$M_{out} = \frac{1}{1+\frac{\pi^2}{4F}\frac{R_{res}}{R_L}}\left(\frac{1}{2}-\frac{2V_f}{V_{in}}\right) \tag{26}$$

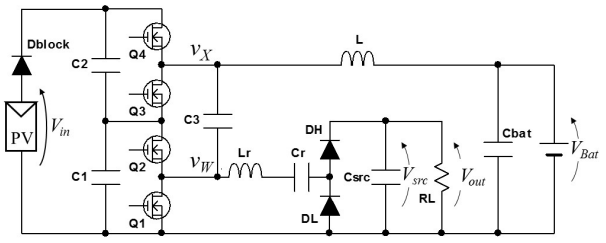

Fig. 21. SC-MPC based on 2s-SCC.

The regulation range of (25) is between 0.5 and 1.0, and is wider than that of (4) (i.e., between 0.33 and 0.67) thanks to the 2s-SCC structure. Meanwhile, M_{out} of (26) is lower than (11) because of the grounded C_{src}. Thus, regulation ranges of M_{bat} and M_{out} can be adjusted and should be properly determined according to applications and requirements.

References

[1] C. Zhao, S. D. Round, and J. W. Kolar, "An isolated three-port bidirectional dc–dc converter with decoupled power flow management," *IEEE Ind. Electron*., vol. 23, no. 5, pp. 2443–2453, Sep. 2008.

[2] H. Tao, A. Kotsopoulos, J.L. Duarte, and M.A.M. Hendrix, "Transformer-coupled multiport ZVS bidirectional dc–dc converter with wide input range," *IEEE Power Electron*., vol. 23, no. 2, pp. 771–781, Mar. 2008.

[3] H. Krishnaswami and N. Mohan, "Three-port series-resonant dc–dc converter to interface renewable energy sources with bidirectional load and energy storage ports," *IEEE Power Electron*., vol. 24, no. 10, pp. 2289–2297, Oct. 2009.

[4] H. A. Atrash, F. Tian, and I. Batarseh, "Tri-modal half-bridge converter topology for three-port interface," *IEEE Trans. Power Electron*., vol. 22, no. 1, pp. 341–345, Jan. 2007.

[5] Z. Qian, O.A. Rahman, H.A. Atrach, and I. Batarseh, "Modeling and control of three-port dc/dc converter interface for satellite applications," *IEEE Trans. Power Electron*., vol. 25, no. 3, pp. 637–649, Mar. 2010.

[6] D. Debnath and K. Chatterjee, "Two-stage solar photovoltaic-based stand-alone scheme having battery as energy storage element for rural deployment," *IEEE Trans. Ind. Electron*., vol. 62, no. 7, pp. 4148–4157, Jul. 2015.

[7] X. Sun, Y. Shen, W. Li, and H. Wu, "A PWM and PFM Hybrid Modulated Three-Port Converter for a Standalone PV/Battery Power System," *IEEE J. Emerging Selected Topics Power Electron*., vol. 3, no. 4, pp. 984–1000, Dec. 2015.

[8] G. J. Su, and L. Tang, "A multiphase, modular, bidirectional, triple-voltage dc–dc converter for hybrid and fuel cell vehicle power systems," *IEEE Trans. Power Electron*., vol. 23, no. 6, pp. 3035–3046, Nov. 2008.

[9] W. Li, J. Xiao, Y. Zhao, and X. He, "PWM plus phase angle shift (PPAS) control scheme for combined multiport dc/dc converters," *IEEE Trans. Power Electron*., vol. 27, no. 3, pp. 1479–1489, Mar. 2012.

[10] H. Wu, K. Sun, R. Chen, H. Hu, and Y. Xing, "Full-bridge three-port converters with wide input voltage range for renewable power systems," *IEEE Trans. Power Electron*., vol. 27, no. 9, pp. 3965–3974, Sep. 2012.

[11] H. Wu, P. Xu, H. Hu, Z. Zhou, and Y. Xian, "Multiport converters based on integration of full-bridge and bidirectional dc–dc topologies for renewable generation systems," *IEEE Trans. Ind. Electron*., vol. 61, no. 2, pp. 856–869, Feb. 2014.

[12] W. Li, C. Xu, H. Luo, Y. Hu, X. He, and C. Xia, "Decoupling-controlled triport composited dc/dc converter for multiple energy interface," *IEEE Trans. Ind. Electron*., vol. 62, no. 7, pp. 4504–4513, Jul. 2015.

[13] J. Zhang, H. Wu, X. Qin, and Y. Xing, "PWM plus secondary-side phase-shift controlled soft-switching full-bridge three-port converter for renewable power systems," *IEEE Trans. Ind. Electron*., vol. 62, no. 11, pp. 7061–7072, Nov. 2015.

[14] Y. Hu, W. Xiao, W. Cao, B. Ji, D. J. Morrow, "Three-port dc–dc converter for stand-alone photovoltaic systems," *IEEE Trans. Power Electron*., vol. 30, no. 6, pp. 3068–3076, Jun. 2015.

[15] M. C. Mira, Z. Zhang, A. Knott, and M. A. E. Andersen, "Analysis, design, modeling, and control of an interleaved-boost full-bridge three-port converter for hybrid renewable energy systems," *IEEE Trans. Power Electron*., vol. 32, no. 2, pp. 1138–1155, Feb. 2017.

[16] P. Yang. C. K. Tse, J. Xu, and G. Zhou, "Synthesis and analysis of double-input single-output dc/dc converters," *IEEE Trans. Ind. Electron*., vol.62, no. 10, pp. 6284–6295, Oct. 2015.

[17] A. Hintz, U. R. Prasanna, and K. Rajashekara, "Novel modular multiple-input bidirectional dc–dc power converter (MIPC) for HEV/FCV application," *IEEE Ind. Electron*., vol. 62, no. 5, pp. 3068–3076, May 2015.

[18] K. Gummi and M. Ferdowsi, "Double-input dc–dc power electronic converters for electric-drive vehicles—topology exploration and synthesis using a single-pole triple-throw switch," *IEEE Trans. Ind. Electron*., vol. 57, no. 2, pp. 617–623, Feb. 2010.

[19] A. Nahavandi, M. T. Hagh, M. B. B. Sharifian, and S. Danyali, "A nonisolated multiinput multioutput dc–dc boost converter for electric

vehicle applications," *IEEE Trans. Power Electron*., vol. 30, no. 4, pp. 1818–1835, Apr. 2015.
[20] M. Marchesoni and C. Vacca, "New dc–dc converter for energy storage system interfacing in fuel cell hybrid electric vehicles," *IEEE Trans. Power Electron*., vol. 22, no. 1, pp. 301–308, Jan. 2007.
[21] R.R. Ahrabi, H. Ardi, M. Elmi, and A. Ajami, "A novel step-up multiinput dc–dc converter for hybrid electric vehicles application," *IEEE Trans. Power Electron*., vol. 32, no. 5, pp. 3549–3561, May 2017.
[22] H. Zhu, D. Zhang, B. Hang, and Z. Zhou, "A nonisolated three-port dc–dc converter and three-domain control method for PV-battery power systems," *IEEE Trans. Ind. Electron*., vol. 62, no. 8, pp. 4937–4947, Aug. 2015.
[23] H. Zhu, D. Zhang, Q. Liu, and Z. Zhou, "Three-port dc/dc converter with all ports current ripple cancellation using integrated magnetic technique," *IEEE Trans. Ind. Electron*., vol. 31, no. 3, pp. 2174–2186, Mar. 2016.
[24] N. Katayama, S. Tosaka, T. Yamanaka, M. Hayase, K. Dowaki, and S. Kogoshi, "New topology for dc–dc converters used in fuel cell–electric double layer capacitor hybrid power source systems for mobile devices," *IEEE Trans. Ind. Appl*., vol. 52, no. 1, pp. 313–321, Jan./Feb. 2016.
[25] H. Nagata and M. Uno, "Multi-port converter integrating two PWM converters for multi-power-source systems," in Proc. *IEEE Int. Future Energy Electron. Conf., IFEEC ECCE-Asia*, pp. 1833–1838, Jun. 2017.
[26] S. R. Sanders, E. Alon, H. P. Le, M. D. Seeman, M. Jhon, and V. W. Ng, "The road to fully integrated dc–dc conversion via the switched-capacitor approach," *IEEE Trans. Power Electron*., vol. 28, no. 9, pp. 4146–4155, Sep. 2013.
[27] Y. Lei, W.C. Liu, and R.C.N.P. Podgurski, "An analytical method to evaluate and design hybrid switched-capacitor and multilevel converters," *IEEE Trans. Power Electron*., vol. 33, no. 3, pp. 2227–2240, Mar. 2018.
[28] A. Lopez, R. Diez, G. Perilla, and D. Patino, "Analysis and comparison of three topologies of the ladder multilevel dc-dc converter," *IEEE Trans. Power Electron*., vol. 27, no. 7, pp. 3119–3127, Jul. 2012.
[29] F. Zhang, L. Du, F. Z. Peng, and Z. Qian, "A new design method for high-power high-efficiency switched-capacitor dc-dc converters," *IEEE Trans. Power Electron*., vol. 23, no. 2, pp. 832–840, Mar. 2008.
[30] D.F. Cortez, G. Waltrich, J. Fraigneaud, H. Miranda, and I. Barbi, "DC–DC converter for dual-voltage automotive systems based on bidirectional hybrid switched-capacitor architectures," *IEEE Trans. Ind. Electron*., vol. 62, no. 5, pp. 3296–3304, May 2015.
[31] M. Evzelman and S.B. Yaakov, "Simulation of hybrid converters by average models," *IEEE Trans. Ind. Appl*., vol. 50, no. 2, pp. 1106–1113, Mar./Apr. 2014.
[32] M. Uno and A. Kukita, "PWM converter integrating switched capacitor converter and series-resonant voltage multiplier as equalizers for photovoltaic modules and series-connected energy storage cells for exploration rovers," *IEEE Trans. Power Electron*., vol. 32, no. 11, pp. 8500–8513, Nov. 2017.
[33] K. I. Hwu and Y. T. Yau, "Resonant voltage divider with bidirectional operation and startup considered," *IEEE Trans. Power Electron*., vol. 27, no. 4, pp. 1996–2006, Apl. 2012.
[34] K. Kesarwani, R. Sangwan, and J.T. Stauth, "Resonant-switched capacitor converters for chip-scale power delivery: design and implementation," *IEEE Trans. Power Electron*., vol. 30, no. 12, pp. 6966–6977, Dec. 2015.
[35] E. Hamo, M. Evzelman, and M.M. Peretz, "Modeling and analysis of resonant switched-capacitor converters with free-wheeling ZCS," *IEEE Trans. Power Electron*., vol. 30, no. 9, pp. 4952–4959, Sep. 2015.
[36] A. Cervera, M. Evzelman, M.M. Peretz, and S.B. Yaakov, "A high-efficiency resonant switched capacitor converter with continuous conversion ratio," *IEEE Trans. Power Electron*., vol. 30, no. 3, Mar. 2015, pp. 1373–1382.
[37] K. Sano and H. Fujita, "Performance of a high-efficiency switched-capacitor-based resonant converter with phase-shift control," *IEEE Trans. Power Electron*., vol. 26, no. 2, pp. 344–354, Feb. 2011.
[38] Y. Lei, C. Barth, S. Qin, W.C. Liu, I. Moon, A. Stillwell, D. Chou, T. Foulkes, Z. Ye, Z. Liao, and R.C.N.P. Podgurski, "A 2-kW single-phase seven-level flying capacitor multilevel inverter with an active energy buffer," *IEEE Trans. Power Electron*., vol. 32, no. 11, pp. 8570–8581, Nov. 2017.
[39] M. Mellincovsky, V. Yuhimenko, M.M. Peretz, and A. Kuperman,, "Low-frequency dc-link ripple elimination in power converters with reduced capacitance by multiresonant direct voltage regulation," *IEEE Trans. Ind. Electron*., vol. 64, no. 3, pp. 2015–2023, Mar. 2017.
[40] M. D. Seeman and S. R. Sanders, "Analysis and optimization of switched-capacitor dc-dc converters," *IEEE Trans. Power Electron*., vol. 23, no. 2, pp. 841–851, Mar. 2008.
[41] B. Oraw and R. Ayyanar, "Load adaptive, high efficiency, switched capacitor intermediate bus converter," in Proc. *IEEE Int. Telecommun. Energy Conf., INTELEC'07*, pp. 1872–1877, Feb. 2007.
[42] G. V. Piqué, H. J. Bergveld, and E. Alarcón, "Survery and benchmark of fully integrated switching power converters: switched-capacitor versus inductive approach," *IEEE Trans. Power Electron*., vol. 28, no. 9, pp. 4156–4167, Sep. 2013.
[43] M. Evzelman and S. B. Yaakov, "Average-current-based conduction losses model of switched capacitor converters," *IEEE Trans. Power Electron*., vol. 28, no. 7, pp. 3341–3352, Jul. 2013.

Masatoshi Uno (M'06) was born in Japan in 1979. He received the B.E. degree in electronics engineering and the M.E. degree in electrical engineering from Doshisha University, Kyoto, Japan, and the Ph.D. degree in space and astronautical science from the Graduate University for Advanced Studies, Hayama, Japan, in 2002, 2004, and 2012, respectively.

In 2004, he joined the Japan Aerospace Exploration Agency, Sagamihara, Japan, where he developed spacecraft power systems including battery, photovoltaic, and fuel cell systems. In 2014, he joined the Department of Electrical and Electronics Engineering, Ibaraki University, Ibaraki, Japan, where he is currently an Associate Professor of Electrical Engineering.

His research interests include switching power converters for renewable energy systems, life evaluation for supercapacitors and lithium-ion batteries, and development of spacecraft power systems. Dr. Uno is a member of the Institute of Electrical Engineers of Japan (IEEJ) and the Institute of Electronics, Information, and Communication Engineers (IEICE).

Kazuki Sugiyama was born in Japan in 1994. He received the B.E. degree and M.E degree in electrical engineering from Ibaraki University, Ibaraki, Japan, in 2016 and 2018, respectively. Since 2018, he has been with East Japan Railway Company.

His research interests include PWM- and PFM-switched capacitor converters for photovoltaic systems.